

1 Wave Spectrum Retrieval from Airborne Sunglitter
2 Images

3 Maria Yurovskaya^{a,b}, Nicolas Rasle^{c,d}, Vladimir Kudryavtsev^{a,b}, Bertrand
4 Chapron^{b,d}, Louis Marie^d, Jeroen Molemaker^d

5 ^a*Federal State Budget Scientific Institution "Marine Hydrophysical Institute of RAS",*
6 *Sevastopol, Russia*

7 ^b*Satellite Oceanography Laboratory, Russian State Hydrometeorological University, Saint*
8 *Petersburg*

9 ^c*Division de Oceanologia, Centro de Investigación Científica y de Educación Superior de*
10 *Ensenada, Baja California, Mexico*

11 ^d*Institut Français de Recherche pour l'Exploitation de la Mer, Plouzané, France*

12 **Abstract**

The method and algorithm development to retrieve the two-dimensional wave spectrum from airborne sunglitter photographs are presented. Based on a linear transfer function deduced from the shape of brightness distribution in the sunglitter zone, the absolute wavenumber elevation spectrum does not require any additional assumption or information about sky brightness, wind or wave energy. A step by step algorithm is given and applied to airborne images taken during an experiment in the Gulf of Mexico. Retrieved spectra agree well with nearby NDBC buoy data, both for spectrum shape, level and energy angular distribution. The 180-degree wave direction ambiguity, inherent to image-derived spectra, is eliminated by using cross-correlation analysis between two consecutive images. A case study corresponding to the spectral evolution with increasing distance from shore in slanting-fetch conditions is then considered. Energy level and peak position transformation agree with established approximations and laws of wind-sea development. The technical

requirements (flight altitude, image resolution, view angles, etc) and applicability of the suggested methodology are discussed. These results demonstrate the potential efficiency of high resolution sea state monitoring from drones or light aircrafts using sunglitter imagery.

13 *Keywords:* sunglitter, sea surface waves, directional wave spectrum, aerial
14 photography, field measurements, remote sensing observations, high
15 resolution, drone

16 **1. Introduction**

17 For a wide range of applications, such as coastal management, the design
18 and operational safety of harbours, ships, and offshore structures, a precise
19 knowledge of the directional spectrum of ocean waves is needed. The di-
20 rectional wave spectrum describes the distributed energy contributions from
21 waves propagating in different directions with different wavelengths. It is key
22 to help determine the consequences of interactions between waves and other
23 structures, i.e. breakwaters and offshore structures, but also to evaluate
24 wave-induced upper ocean transport and erosion processes.

25 Significant advances have thus been made to estimate these directional
26 wave statistical properties. Today, a large number of measuring devices,
27 working on different principles, are available (e.g. Herbers et al., 2012). Yet,
28 the directional and frequency response of these systems may often be limited
29 and not sufficient to fully resolve directional surface wave spectra. Further,
30 requirements for near-simultaneous, high spatial resolution observations, to
31 provide more direct directional wavenumber measurements of the local sur-
32 face field over entire regions, has attracted the attention on remote sensing

33 technologies. To complement sparse in-situ buoy measurements, techniques
34 can include sea level radars (coastal HF radars, Barrick and Lipa, 1985),
35 microwave and marine X-band radars (Senet et al., 2008; Nieto et al., 2004),
36 scanning altimeter and lidar high-resolution topography instruments from
37 airplane platforms (Walsh et al., 1998; Melville et al., 2016), and also syn-
38 thetic aperture or rotating real-aperture airborne radar instruments (Caudal
39 et al., 2014). As well, photographs of the ocean surface have long been
40 proved to contain quantitative information about ocean surface slope statis-
41 tics (e.g. Barber, 1949; Cox and Munk, 1956), to help infer directional spectra
42 of surface waves (Stilwell, 1969; Stilwell and Pilon, 1974). Today, with the
43 significant cost reduction and improvement of both instruments and drones,
44 the photograph techniques may become more widely used to observe and
45 monitor surface waves at regional or coastal scales.

46 Since almost two centuries (Spooner, 1822), it has been understood that
47 the shape of the sunglint on the sea surface contains information on the
48 statistical properties of wave slopes. Airborne and satellite sunglint images
49 at medium (~ 1 km) resolution have then been used to precisely estimate
50 sea surface slope statistical properties (Cox and Munk, 1956; Breon and
51 Henriot, 2006), and modulations by various dynamical ocean processes like
52 currents and fronts, internal waves, or surface slicks (Barber, 1954; Apel
53 et al., 1975; Hennings et al., 1994; Kudryavtsev et al., 2012; Kudryavtsev
54 et al., 2012; Rascle et al., 2016, 2017). At higher ($\sim 1 - 10$ m) resolution,
55 glitter modulations are more directly connected to the wavy surface. Indeed,
56 wave contrasts on the image result from the modulation of sun reflected
57 radiation by individual tilting wave slopes, and those can be used to estimate

58 the wave directional elevation spectrum (Stilwell and Pilon, 1974; Monaldo
59 and Kasevich, 1981).

60 To derive wave elevations from these brightness variations, a transfer
61 function must thus be determined. Using airborne photographs, this task is
62 eased, as the overall sunglitter shape can be captured, to help directly infer
63 a linear transfer function (Bolshakov et al., 1988). Adapted to a satellite
64 configuration, such a method was successfully applied (Kudryavtsev et al.,
65 2017a,b) to reconstruct the spectrum of long (energy containing) waves from
66 satellite sunglitter images, taking advantage of the high resolution and spe-
67 cific viewing geometry of the radiometers on-board the satellite Sentinel-2.

68 In this paper, we further dwell on this capability of airborne sunglitter
69 imagery to provide the overall glitter pattern. As mentioned above, this
70 property provides direct means to determine a linear transfer function. Our
71 motivation is then to further assess how robust is our proposed methodology
72 to efficiently provide quantitative estimates of the directional wave spectrum,
73 including energy containing waves and also short waves. The development
74 is specific to airborne measurements and applied to data collected over a
75 coastal area in the northern Gulf of Mexico.

76 The paper structure is as follows. The experiment is described in Sec-
77 tion 2; theory and spectrum reconstruction algorithm are presented in Sec-
78 tion 3; method implementation and validation are given in Section 4; the
79 results of the study of wave development and transformation with fetch are
80 presented in Section 5, and finally, the discussion of method applicability and
81 some recommendations on experimental setup are suggested in Section 6.

82 2. Experiment and Data

83 The airborne sunglitter images were obtained on Jan. and Feb. 2016
84 during the Lagrangian Submesoscale Experiment (LASER), where a large
85 number (~ 1000) of surface drifters were deployed to study surface dispersion
86 within the Gulf of Mexico (D’Asaro et al., 2018; Raschle et al., 2017), close to
87 the site of the Deep Horizon oil platform accident in 2010 (Fig. 1, a). The
88 images were acquired from airplane (a Partenavia P.68) flying at altitudes
89 up to 3000 m.

90 The visible light intensity was measured by two panchromatic cameras
91 (JAI BM-500GE) equipped with a 5 mm focal length low distortion lens to
92 ensure a large field of view. The cameras setup is sketched in Figure 1, b. To
93 capture the sunglint, the two cameras were arranged symmetrically about
94 the airplane nadir with a pitch of $\pm 35^\circ$ for the forward/aftward cameras.
95 The camera aperture angles are $80^\circ \times 70^\circ$ along-track and across-track, re-
96 spectively, with 2456×2058 pixels in the respective directions. For a flight
97 altitude of 1000 m, this leads to a ground resolution from 0.5 m to 6 m. The
98 cameras acquired images at 2 Hz. The images were geolocated using an in-
99 ternal motion unit Applanix POS AV V610.

100 We selected cases corresponding to measurements made during flights
101 with trajectories close to National Data Buoy Center (NDBC) buoy locations,
102 to benefit from synchronous wind and wave ancillary data. A step by step
103 algorithm is provided for images obtained close to NDBC 42012 in developed
104 wind sea conditions on 11-Feb-2016 (green star on Fig. 1, a). Further we
105 analyze the wave evolution on 23-Jan-2016, when sunglitter images were
106 acquired (in cloudless regions) at different distances from the shore along the

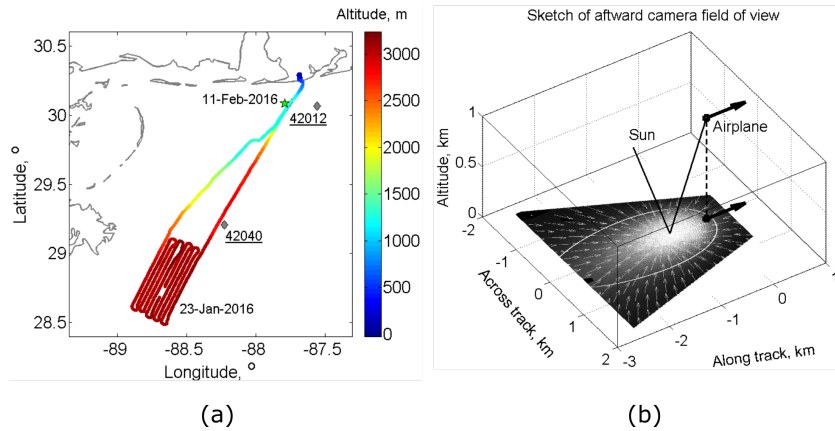


Figure 1: (a) The observation area with NDBC buoy locations (gray diamonds). Green star shows location of the analysis on 11-Feb-2016 (section 4), colors are the tracks of the 23-Jan-2016 flight (section 5). (b) Sketch of the field of view of the afterword camera, for a flight altitude of 1000 m. Here we show the special case of the sun exactly at the rear of the airplane when the specular sun spot is at the center of the camera field of view. The ellipse is the contour $Z_n^2 = s^2$ (see the notifications below). The white arrows show the orientations of the transfer function gradient, G_{zi} .

107 plane tracks shown in Fig. 1, a.

108 3. Theoretical Background

109 Based on the classical model of the sea surface brightness formation in the
 110 visible range (Cox and Munk, 1956), the intensity in each pixel of sunglitter
 111 image is proportional to the sun reflected radiance, or the energy brightness
 112 of the surface (the spectral energy flux per unit area per unit solid angle):

$$N = \frac{\rho E_s}{4 \cos \theta \cos^4 \beta} P(Z_1, Z_2), \quad (1)$$

113 where P is the probability density of two slope components, Z_1, Z_2 , satisfying
 114 the conditions of specular reflection:

$$\begin{aligned} Z_1 &= -\frac{\sin \theta_s \cos \phi_s + \sin \theta \cos \phi_\nu}{\cos \theta_s + \cos \theta} \\ Z_2 &= -\frac{\sin \theta_s \sin \phi_s + \sin \theta \sin \phi_\nu}{\cos \theta_s + \cos \theta}, \end{aligned} \quad (2)$$

115 θ and θ_s are zenith angles for the camera and the sun, respectively, ϕ_ν and
 116 ϕ_s are corresponding azimuth angles, ρ is the Fresnel reflection coefficient,
 117 E_s is the solar radiance, $\tan \beta = \sqrt{Z_1^2 + Z_2^2}$.

118 Local modulations of $B = N \cos \theta / \rho$, or equivalently, of P , can arise for
 119 two reasons: variations of the slope statistics mostly governed by changes
 120 of mean square slope (MSS) due to different upper ocean processes (fronts,
 121 internal waves, surface slicks, etc), or the tilting of the ocean surface while a
 122 long wave is propagating. The latter can also lead to a short wave (and thus,
 123 MSS) modulation along the wave profile. As demonstrated by Bolshakov
 124 et al. (1988) and Kudryavtsev et al. (2017a), one can ignore these MSS
 125 modulations in the vicinity of brightness contrast inversion zone, i.e. $0.5 <$
 126 $Z_n^2 / s^2 < 2$, where $Z_n^2 = Z_1^2 + Z_2^2$, and s^2 is the surface MSS to the first order
 127 estimated from the assumption of Gaussian brightness and slope distribution
 128 as $s^2 = -2\overline{Z_n} \cdot \overline{B} / (\partial B / \partial Z_n)$. The brightness variation due to the long wave
 129 propagation then writes:

$$\tilde{B} = B(Z_1 + \zeta_1, Z_2 + \zeta_2) - B(Z_1, Z_2) = \frac{\partial B}{\partial Z_i} \zeta_i \equiv G_{zi} \zeta_i, \quad (3)$$

130 where $\zeta_{1,2}$ are the components of tilting wave slope. G_{zi} is the transfer
 131 function, relating brightness and slope variations. This transfer function is

132 then determined as the brightness gradient in specular slope space and can
 133 be obtained through the observed brightness gradients:

$$\begin{aligned} G_{z1} &= (G_2 Z_{2,1} - G_1 Z_{2,2})/\Delta \\ G_{z2} &= (G_1 Z_{1,2} - G_2 Z_{1,1})/\Delta, \end{aligned} \quad (4)$$

134 where $G_i = \partial B/\partial x_i$, $Z_{i,j} = \partial Z_i/\partial x_j$, $\Delta = Z_{1,2}Z_{2,1} - Z_{1,1}Z_{2,2}$.

135 From (3), the relation between elevation and brightness spectra thus
 136 writes :

$$S_\zeta(\mathbf{k}) = S_B(\mathbf{k})/(G_{zi}k_i)^2. \quad (5)$$

137 The linear combination of wave vector components in the denominator
 138 of (5) vanishes in a direction perpendicular to the gradient direction. Close
 139 to this direction, the spectrum cannot be simply retrieved. As suggested
 140 by Bolshakov et al. (1988) and also Lupyan (1988), this singularity can be
 141 eliminated, by using several image fragments with different gradients G_{zi}^n ,
 142 but statistically identical wave spectrum, $S_\zeta^n(\mathbf{k}) = S_\zeta(\mathbf{k})$. As sketched in
 143 Fig. 1, b, where the typical distribution of G_{zi}^n orientations is shown, the
 144 vectors converge towards the sunlitter center, changing their direction from
 145 0° to 360° around it. Brightness spectra taken from fragments with different
 146 vector orientations can then be averaged, to obtain the elevation spectrum
 147 without any singularity:

$$S_\zeta(\mathbf{k}) = \sum_{n=1}^N S_B^n(\mathbf{k}) / \sum_{n=1}^N (G_{zi}^n k_i)^2. \quad (6)$$

148 As described, the considered methodology is self-consistent, solely based
149 on the transfer function estimation from the observed shape of solar glint.
150 For airborne photography, the following steps must then be taken:

- 151 • gradients G_i , $Z_{i,j}$ are determined from the smoothed sunglitter pattern
152 and known geometrical parameters;
- 153 • a transfer function, G_{zi} , is calculated using (4);
- 154 • several image fragments are selected in different image parts, still in
155 the vicinity of contrast inversion zone, and their brightness spectra are
156 calculated;
- 157 • the absolute directional wave elevation spectrum is derived from the
158 sum of brightness spectra and transfer function field, using expression
159 (6);
- 160 • 180-degree wave direction ambiguity can be removed using cross-correlation
161 analysis of two consequent images.

162 A detailed example of airborne sunglitter image processing is given below.

163 4. Method Implementation

164 4.1. Image preprocessing

165 On 11-Feb-2016, a snapshot of the sea surface (Fig. 2, a) was extracted
166 close to the location of the NDBC buoy number 42012 (Fig. 1, a). The wind
167 was about 9 m s^{-1} blowing from South-West, and peak waves of about 40 m
168 wavelength were propagating from the same direction.

169 The above procedure must be applied to a brightness field predominantly
 170 formed by the sunlight reflections from the sea surface. Besides the image
 171 projection onto the sea surface plane (Fig. 2, b), a preparatory step is to
 172 consider an intensity correction to possibly account for extraneous factors
 173 hampering the image brightness. We neglect any vignetting effect and con-
 174 sider the image intensity proportional to the energy surface brightness, N .
 175 First, the sky reflection and scattered radiation can contribute to the image
 176 brightness. Cox and Munk (1956) report corresponding dependencies on in-
 177 cidence angle by considering intensities from regions far outside the glitter.
 178 A similar procedure is to use the darkest column of the photograph (the right
 179 one in the example on Fig. 2, a). Given the viewing geometry and neglect-
 180 ing the sunlitter contribution within this darkest line, the incidence angle
 181 dependency of the background radiance can be estimated. A correspond-
 182 ing polynomial approximation, Fig. 2, c, is then assumed to extend over the
 183 whole 2D image, and further subtracted. Nevertheless, in all considered ex-
 184 amples, we do not use parts of the images with $\theta > 50^\circ$, areas over which the
 185 impact of scattered radiation rapidly grows (Cox and Munk, 1956), and the
 186 assumption (3) loses its validity.

187 According to (1), the detrended field, $N - N_{back}$ (not shown), should
 188 be multiplied by $\cos\theta/\rho$, shown in Fig. 2, d. Values of $\cos\theta/\rho$ differ up
 189 to 4-5 times on the opposite image borders with incidence angles 25° and
 190 60° . This operation suppresses the brightness of the distant zone and shifts
 191 the sunlitter center towards the edge corresponding to the lowest incidence
 192 angle (compare Fig. 2, b and Fig. 2, e). The mean brightness field, B_0
 193 (Fig. 2, f), is then derived by smoothing $B = (N - N_{back}) \cos\theta/\rho$ using a

194 moving average filter, with a window size depending on the image resolution
195 (about several lengths of dominant wave). All the algorithm steps then apply
196 to the brightness variation field, $B - B_0$.

197 *4.2. Spectrum validation*

198 A fragment of the brightness variation field is shown Fig. 3, a. Fragments
199 are taken between the two ellipses indicating the zone $0.5 < Z_n^2/s^2 < 2$, and
200 above the line $\theta = 50^\circ$.

201 Fig. 3, b displays the sum of directional brightness spectra. As expected,
202 the resulting transfer function, $\sum(G_{zi}^n k_i)^2$ (Fig. 3, c), does not vanish in
203 any particular direction, but tends to zero in the wavenumber plane center.
204 This may enhance noise level and errors at the lowest wavenumbers. After
205 application of the transfer function, Fig. 3, d, both brightness and wave
206 elevation spectra possess a distinct spectral peak, visually corresponding to
207 the waves observed on the fragment, Fig. 3, a, but the angular distribution
208 of the elevation spectrum is apparently broader, possibly revealing waves
209 moving closer to zonal (eastward or westward) directions.

210 The comparison with the nearby NDBC buoy wavenumber directional
211 spectrum (Fig. 3, d), calculated with the use of the maximum entropy method
212 (Lygre and Krogstad, 1986) and linear dispersion relation for gravity waves,
213 gives a satisfactory agreement of 2D energy distribution. Notice that in
214 contrast to NDBC data that provides a “true” directional spectrum, the
215 spectrum retrieved from the image is folded ($S(\phi) = S(\phi) + S(\phi + 180^\circ)$)
216 having a 180-degree ambiguity in wave direction.

217 Omnidirectional spectra are compared in Fig. 3, f, and give an excellent
218 agreement of peak position and its energy level. Energy underestimation

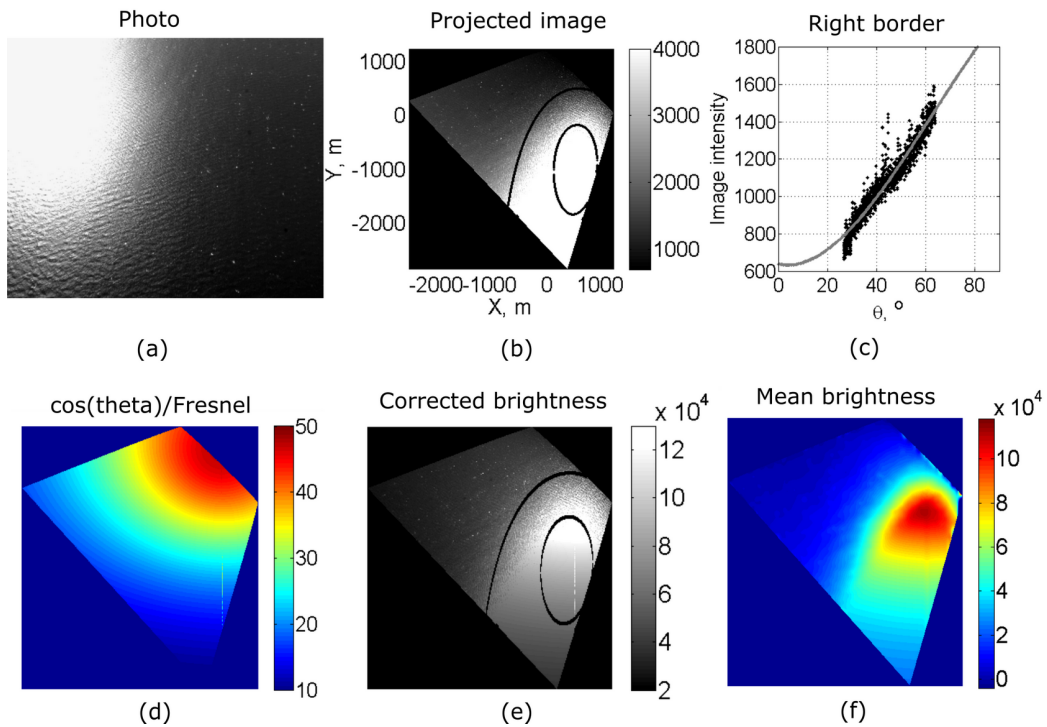


Figure 2: (a) An airborne snapshot of a sea surface; (b) image projected on the sea surface plane (x-label is to the East, y-label is to the North, two ellipses determine the zone $0.5 < Z_n^2/s^2 < 2$); (c) pixel intensities for the left column of a photo (dots) and their polynomial approximation indicating the background radiation; (d) $\cos \theta/\rho$ field; (e) $B = (N - N_{back}) \cos \theta/\rho$ field; (f) mean brightness field, B_0

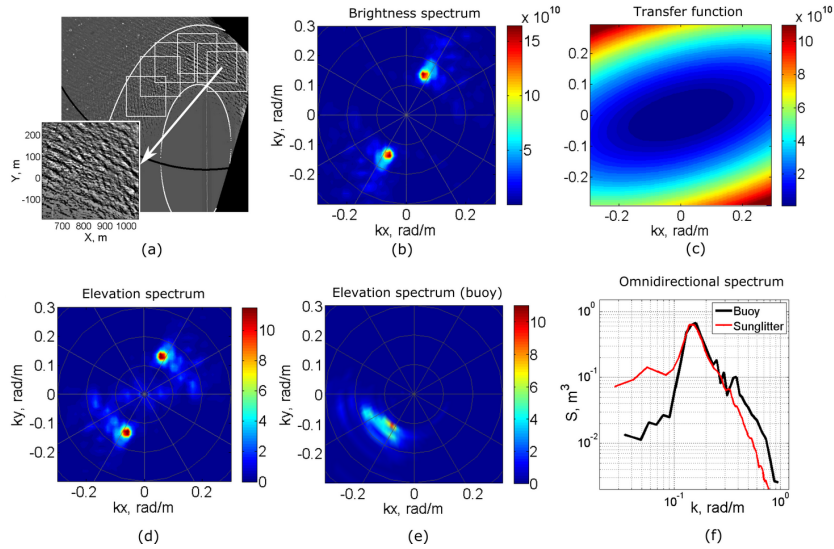


Figure 3: (a) Square fragments (450 m size) of brightness variation field, $(B - B_0)$, taken for spectrum retrieval. Two ellipses determine the zone $0.5 < Z_n^2/s^2 < 2$, black line is $\theta = 50^\circ$; (b) The sum of brightness spectra; (c) the transfer function, $\sum_{n=1}^N (G_{zi}^n k_i)^2$; (d) retrieved from (6) elevation spectrum; (e) NDBC buoy data directional spectrum (42012); (f) Omnidirectional spectra comparison.

219 of retrieved spectrum at wavenumbers $k > 0.3$ rad/m can be explained by
 220 the actual (not interpolated) image resolution and smoothing of features
 221 smaller than 10 m. The noise level at $k < 0.1$ rad/m depends on the B_0
 222 calculation (the smaller the filter window size, the lower the spectrum), and
 223 is also controlled by the singularity of a transfer function around $k = 0$ rad/m.
 224 Energy distribution of waves in a range 20 m - 60 m is reliably reproduced.

225 4.3. Wave direction ambiguity

226 In our cases, the camera acquired images every 0.5 s. Consecutive snap-
 227 shots can then be analyzed to remove the wave propagation directional

228 ambiguity (Fig. 3, d), as already demonstrated for satellite measurements
 229 (Kudryavtsev et al., 2017a; De Michele et al., 2012). Two images of the
 230 same square region of the sea surface taken with a $\Delta t = 0.5$ s time difference
 231 are shown on Fig. 4, a-b. Their spectral coherence, $\langle \hat{I}_2 \hat{I}_1^* \rangle^2 / (\langle \hat{I}_1 \hat{I}_1^* \rangle \langle \hat{I}_2 \hat{I}_2^* \rangle)$,
 232 hat means the Fourier transform, a star is complex conjugation,
 233 and phase, $\arg(\langle \hat{I}_2 \hat{I}_1^* \rangle)$, are given in Fig. 4, b-c. The coherence level is
 234 high, up to 1, in the direction where the waves are observed. The phase
 235 spectrum is a-priori asymmetric, and the positive phase shift corresponds to
 236 the direction “from” in a case when I_1 is taken earlier than I_2 . Thus, the
 237 wave system is moving from South-West, to agree with the NDBC directional
 238 spectrum (fig 3, b).

239 Airborne image time series can further be used to estimate ocean surface
 240 currents from the dispersion of the detected gravity waves (e.g. Dugan and
 241 Piotrowski (2003)). Taking a transect in the phase spectrum, $\Delta\Phi$, along a
 242 direction corresponding to maximum coherency, marked with a dashed line
 243 in Fig. 4, the dispersion can be evaluated for the relative projection of the
 244 phase velocity: $c(k) = \frac{\Delta\Phi/\Delta t}{k}$. As obtained, Fig. 4, e, experimentally derived
 245 points lie very close to the standard prediction, $c = \sqrt{g/k}$, even at large
 246 wavenumbers for which the elevation spectral analysis is less reliable. This
 247 indicates the absence of surface current, or at least its component along the
 248 chosen direction, in the region of observation.

249 5. A Case Study: Spectrum Evolution with Fetch

250 On 23-Jan-2016, an experiment to study wave transformation at varying
 251 distance from the shore was conducted. The airplane moves seawards across

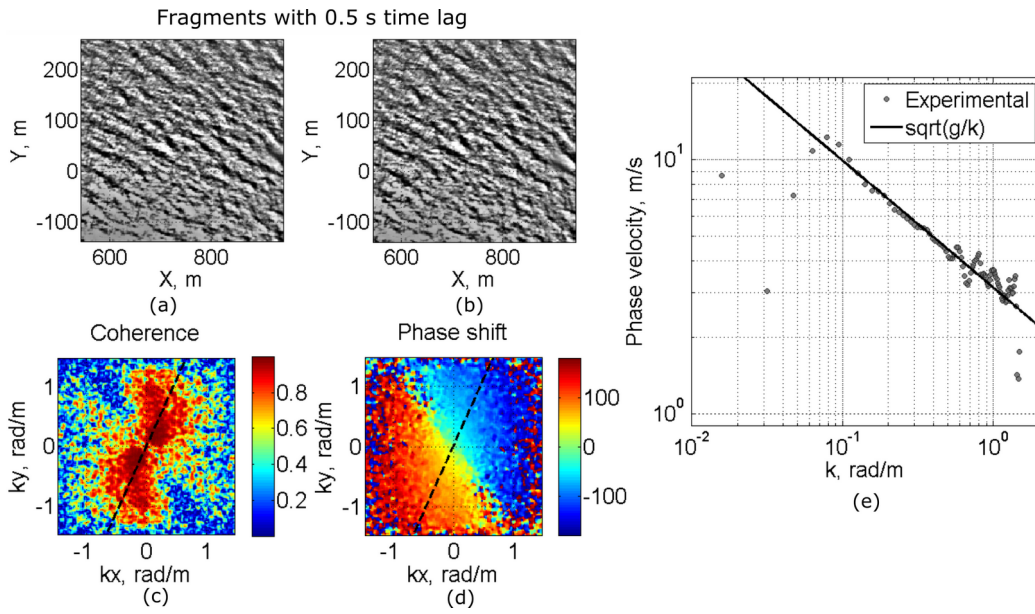


Figure 4: (a)-(b) Snapshots of the same location taken with 0.5 s time shift; (c) coherence of two brightness fields; (d) phase shift; wave direction (from) corresponds to positive values of a phase shift; (e) dispersion relation calculated from a phase shift along the line of coherence maximum (dashed lines in (c) and (d) plots).

252 the NDBC 42012 and 42040 locations (Fig. 1, a, and Fig. 5). The flight
253 started at 19:20 UTC in clear sky conditions, but at 19:31 the plane entered
254 a cloudy zone with gleam areas too small to estimate the wave spectrum. Yet,
255 two images at 19:50 could be exploited. On the way back, at 23:00, camera
256 pitch and sun elevation angle didn't satisfy the condition $Z_n^2/s^2 < 2$ and
257 clouds were still hindering the glitter. As a result, only one image fragment
258 from the glint periphery could be used, with relatively low reliability.

259 The wind speed and direction (in nautical system) around the time of
260 acquisition are plotted in Fig. 6. Wind was blowing from the North-West,
261 slightly rotating clockwise and calming down from 12 m s^{-1} to 10 m s^{-1} ,
262 accordingly to NDBC 42040 data. The slow clockwise wind rotation took
263 place during the previous two days, starting to blow from South, then West,
264 before finally subsiding to 3 m s^{-1} from North on 24-Jan.

265 The two-dimensional slope spectra (Sk^2) from the buoys are shown in
266 Fig. 6. The slope spectra, reconstructed from the airplane images are shown
267 in Fig. 7, for the points marked by red squares on the map of Fig. 5. Many
268 different wave systems co-exist in the area (see sketch Fig. 5).

269 First, there is a long ($k \sim 0.05 \text{ rad m}^{-1}$) swell from West-South-West,
270 probably originating from West of the Mississippi delta and entering the area
271 from the South-West. This swell is well observed at buoy 42040 (Fig. 6,
272 bottom right) and on the airplane spectra at 22:50 (Fig. 7). The North of
273 the bay is probably partially sheltered from that swell, which is weaker seen
274 on the 42012 buoy data (Fig. 6, bottom left) as a Southern swell, though a
275 well-distinguished peak is resolved on omnidirectional spectrum (black and
276 gray curves in Fig. 8 before 19:31). Also, that swell is not properly resolved

277 by the smaller image fragments (due to lower plane altitude, see Fig. 1) used
278 around buoy 42012.

279 Second, there is the wind sea at short wavenumbers ($k > 0.1 \text{ rad m}^{-1}$).
280 The peak of the wind sea is slightly more from the North than the wind
281 direction (marked by a white dashed line in Fig. 6 and Fig. 7), both on buoy
282 data and on the airplane spectra. Third, there is a series of spectral peaks
283 from West to North-West (see before 19:31 on Fig. 7, see also buoy data on
284 Fig. 6). Those peaks are typical of slanting fetch conditions (Ardhuin et al.,
285 2007, e.g.), where the wind sea separates between subsystems, the high-
286 frequency remaining downwind whereas waves at relatively lower frequency
287 develop and propagate in the slanting fetch direction (along-shore). Very
288 close to the shore (before 19:25 on Fig. 7), those slanting short waves even
289 dominate the wind sea spectrum.

290 From the analyzed spectra, the main tendency is a gradual peak shift-
291 ing towards lower wavenumbers and a corresponding energy growth with the
292 fetch distance. These effects are better identified in omnidirectional spectrum
293 evolution, Fig. 8. The figure presents angle-integrated surface elevation spec-
294 trum (red) together with buoy-derived spectra at 19:00 (t1, black) and 20:00
295 (t2, gray) for NDBC 42012, and at 21:00 (t1) and 23:00 (t2) for NDBC 42040.
296 To help the interpretation, empirical model spectra, as suggested by Donelan
297 et al. (1985) and Babanin and Soloviev (1998), are displayed, for different
298 fetches (given in figure titles). Fetches are calculated as the distance to the
299 line passing through alongshore islands (bold green on Fig. 5) in the direc-
300 tion of the wind taken from the nearest buoy. They are further corrected to
301 account for the direction of the spectral peak mostly deviating from NDBC

302 wind direction. At small fetches (below 5-10 km), the spectrum is rather
 303 variable in energy level and peak position, also probably due to the changing
 304 bottom topography and consequent refraction effects. The wind wave peak
 305 is hardly distinguished and only starts to be clearly obtained at fetch about
 306 10 km. At 19:25:31, the fetch value is close to the one captured at NDBC
 307 42012 location (see Fig. 5). The respective spectra are then found very close
 308 (compare black and red curves in Fig. 8). The evolution then continues and
 309 closely follows Donelan et al. (1985) and Babanin and Soloviev (1998) pre-
 310 dictions. Despite the low reliability for the sunlitter-derived spectrum at
 311 22:50 (the last subplot), a good agreement is found with both model and
 312 buoy data taken at approximately the same fetch.

313 To generalize the wind sea peak transformation, we present (Fig. 9, a)
 314 the dependency of dimensionless peak frequency, $f_p u_{10}/g$, and dimensionless
 315 energy, Eg^2/u_{10}^4 , estimated as the spectrum integral around the wind wave
 316 peak and shorter waves, on dimensionless wave fetch, Lg/u_{10}^2 . Comparison is
 317 made with other data collected by Babanin and Soloviev (1998). As obtained,
 318 results are consistent with the cited approximations, except for the wave
 319 energy at the near-shore points. For these cases, the wind peak wavelength
 320 is not far from the camera resolution.

321 The present data, unfortunately, cannot trace any pronounced tendency
 322 for the angular distribution evolution. This is due to the presence of sev-
 323 eral swell peaks much stronger than the wind ones, and inaccurate data at
 324 large fetches, where the wind peak dominates. Yet, the average angular
 325 distribution around the peak wavenumber (Fig. 9, b) does not contradict
 326 the dependency, $S(k_p) = 0.5\beta/\cosh^2(\beta\phi)$, $\beta = 2.28$, reported by Donelan

327 et al. (1985), confirming that multi-modal spectrum structure provides some
328 broadening at the angles far from $\phi = 0$ (peak position).

329 **6. Method Applicability and Constraints**

330 As demonstrated, the proposed spectral reconstruction robustly applies
331 when several requirements are satisfied.

332 The photograph should contain a part of sunglitter ellipse, $Z_n^2 = s^2$,
333 within the camera incidence angle range $\theta < 50^\circ$. The area must be large
334 enough to provide sufficient angle diversity between the transfer function vec-
335 tors that are about normal to the ellipse. This ensures to properly eliminate
336 the singularity of the transfer function. The brightness of the observed area
337 should not be saturated. A saturation shortens the range of slope values.
338 Clouds are also to avoid. Cloudiness, or other inhomogeneities, impact the
339 estimation of the mean brightness characteristics.

340 The question of the impact of wave breaking is still open. Breakers
341 can appear on the image as bright spots, to possibly distort the retrieved
342 slope/elevation distribution. Under high-wind conditions, individual break-
343 ers shall be excluded, and individual breaking crests possibly interpolated.

344 Coming back to the part of the sunglint where the spectrum can be de-
345 rived, i.e. $0.5 < Z_n^2/s^2 < 2$ and $\theta < 50^\circ$, a simplified one-dimensional analysis
346 leads to a necessary condition for the camera zenith angle: $\beta_1 < |\theta - \theta_s| < \beta_2$,
347 where $\beta_1 = 2 \arctan \sqrt{0.5s^2}$, $\beta_2 = 2 \arctan \sqrt{2s^2}$ with $s^2 = 0.003 + 0.00512U_{10}$
348 (Cox and Munk, 1956). Close to the camera nadir direction (Fig. 1), the
349 distance between the two curves represents the longest wavelength being de-

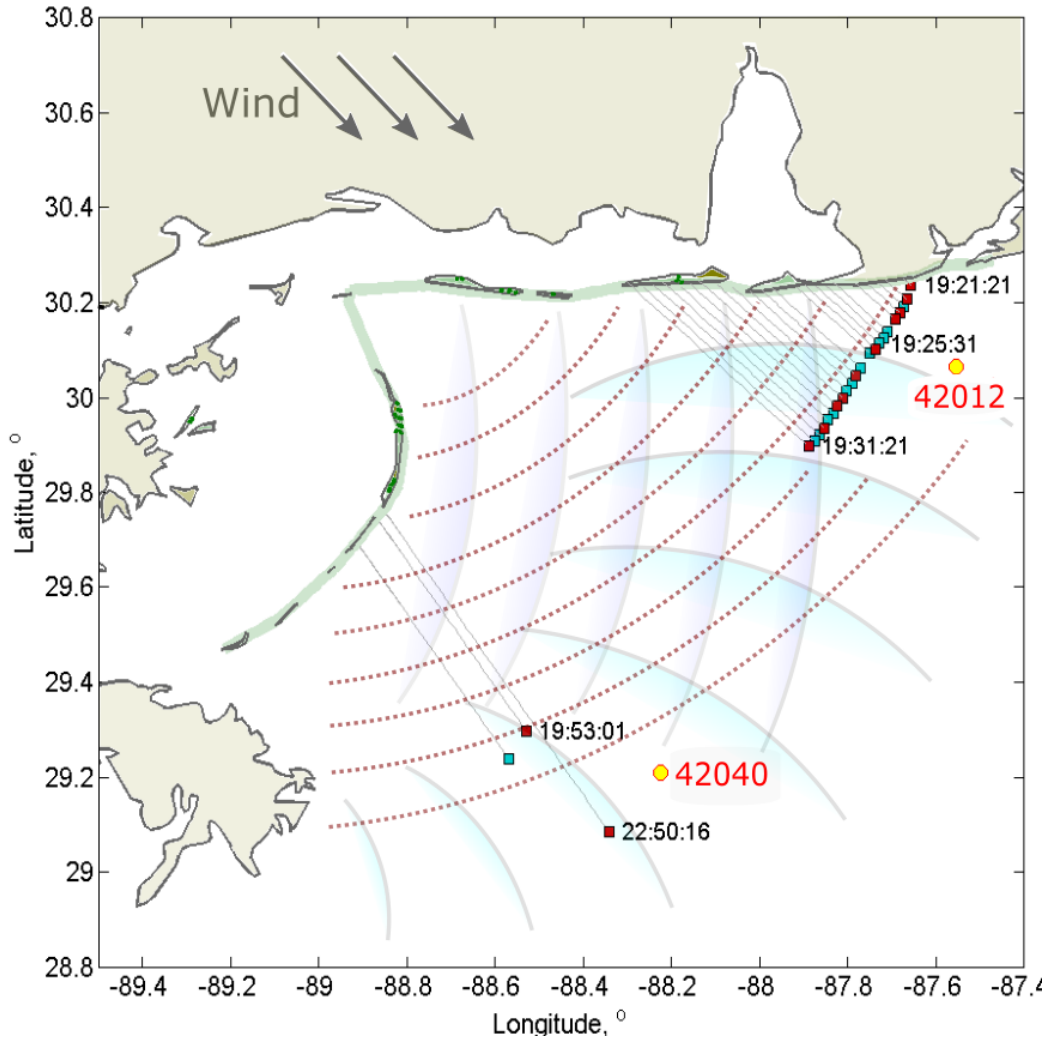


Figure 5: Locations of the images acquired on 23-Jan-2016 near NDBC buoys 42012 and 42040, and schematic wave systems orientations.

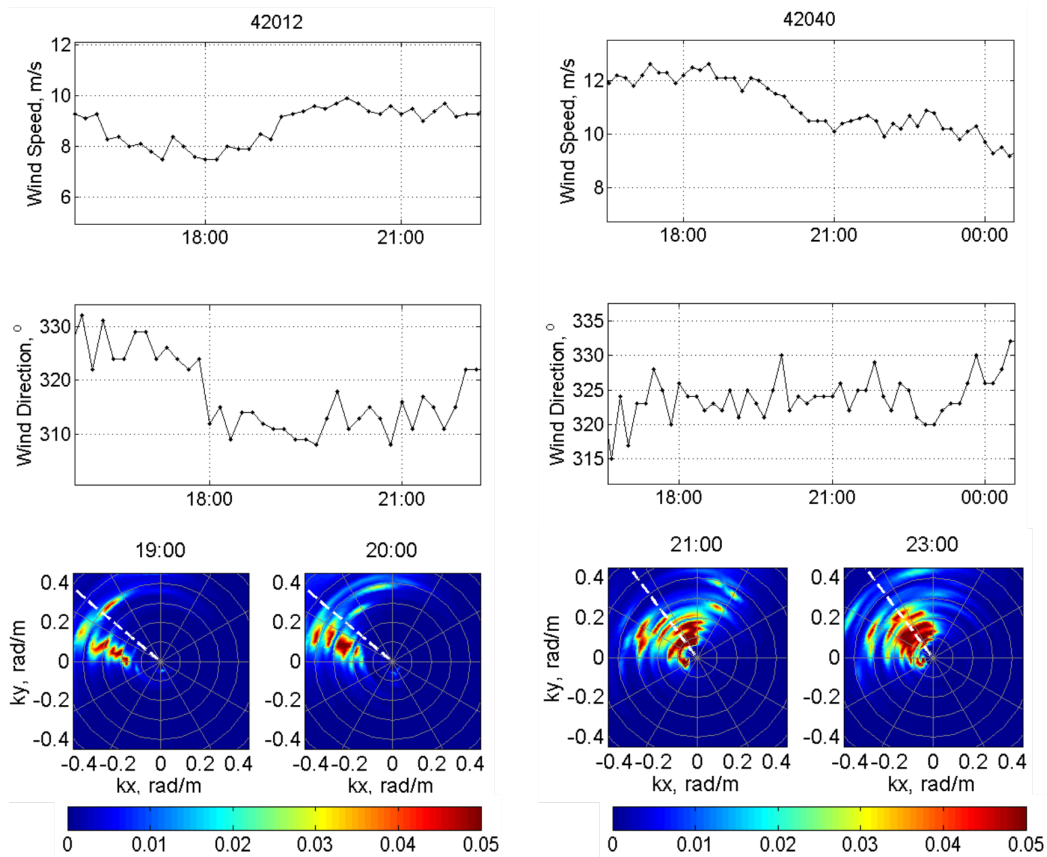


Figure 6: Windspeed, wind direction and directional slope spectra from NDBC 42012 and 42040 buoys around the time of airplane flight. Wind and wave directions are ‘from’ in nautical system.

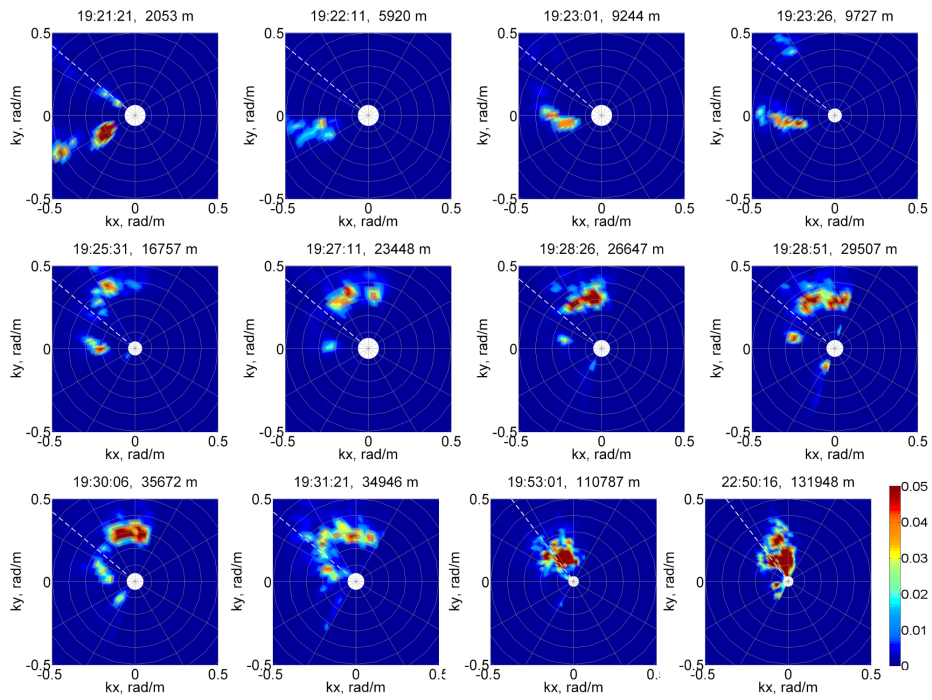


Figure 7: Directional slope spectra at the points marked by red squares on fig 5. White line is the wind direction from buoy data (trigonometrical system). Spectrum develops in presence of swell from West. Wind wave peak grows and shifts towards low wavenumbers, slightly deviates from NDBC wind direction (actually the wind also changed its direction).

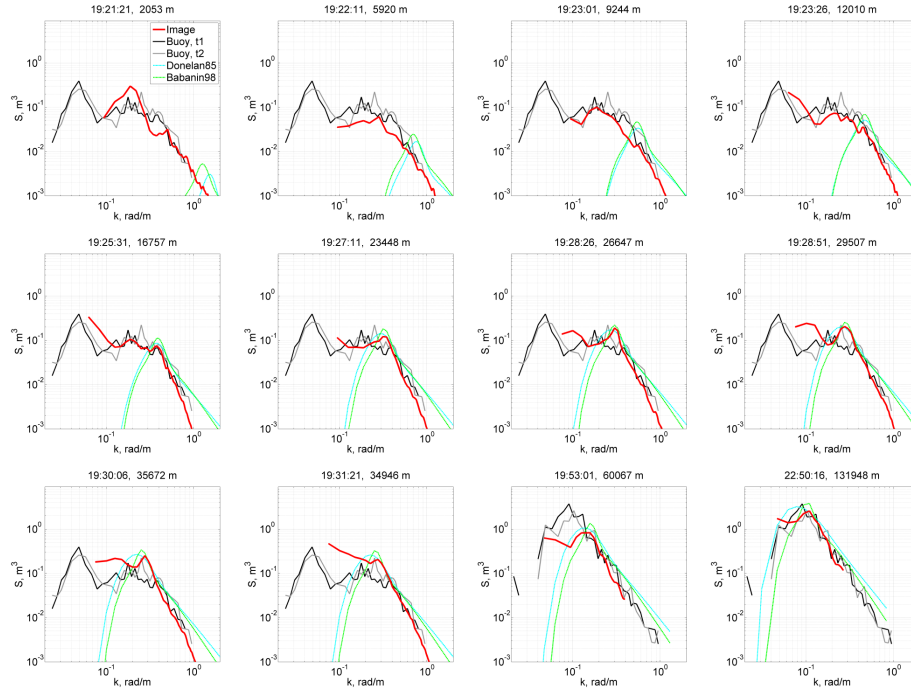


Figure 8: Omnidirectional spectra at the points marked by red squares on fig 5. Wind peak grows and shifts towards lower wavenumbers in consistence with Donelan et al. (1985) and Babanin and Soloviev (1998) spectra. Blue (Babanin and Soloviev, 1998) and green (Donelan et al., 1985) curves are given for the wind speed taken from the nearest buoy (42012 or 42040) and the fetch is corrected accounting for the spectrum wind wave peak direction estimated from Fig. 7.

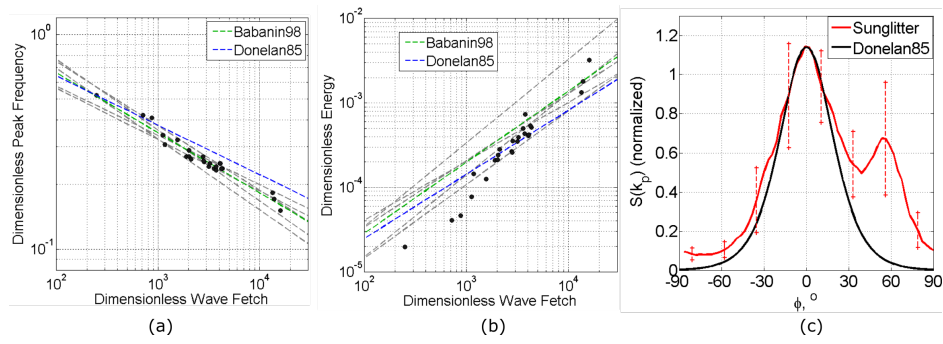


Figure 9: (a) Dimensionless peak frequency vs. dimensionless fetch. Black circles – experimental points (all retrieved spectra), dashed lines – approximations from other authors (Davidan, 1980; Babanin and Soloviev, 1998; Donelan et al., 1985; Kahma, 1981; Dobson et al., 1989; Wen et al., 1989; Ewans and C. Kibblewhite, 1990) for the wind speed 9 m s^{-1} ; (b) Dimensionless peak frequency vs. windsea dimensionless variance with the same notations; (c) angular function suggested by Donelan et al. (1985) and ensemble average wave energy distribution around the peak wavenumber ($0.75k_p < k < 1.25k_p$); the length of vertical lines is equal to standard deviation.

350 tected,

$$d_{long} = H [\tan(\theta_s - \beta_1) - \tan(\theta_s - \beta_2)], \quad (7)$$

351 where H is the plane altitude.

352 The shortest wavelength being detected depends on the camera technical
353 parameters, the camera view angle, γ , and the image pixel size, N_p . The 1D
354 spatial resolution, the Nyquist wavelength, in and around the vicinity of the
355 lens optical line-of sight axis, reads:

$$d_{short} = \frac{4H \tan(\gamma/2)}{N_p \cos \theta}, \quad (8)$$

356 for an altitude H and zenith angle θ .

357 Values of d_{long} for different sun zenith angles and different wind speeds,
358 and of d_{short} for $N_p = 1000$, different camera view angles and two boundary
359 camera zenith angles θ (nadir and 50°), are presented in Fig 10, a, b, as
360 functions of camera altitude. It summarizes the range of wave scales that
361 can be resolved from a sunglitter photograph. In practice, this range is sig-
362 nificantly reduced. For the upper limit, a reliable spectrum estimation shall
363 require a window size to encompass at least three wavelengths, or more,
364 when considering the singularity of the transfer function around zero. The
365 practical maximum wavelength is thus much shorter than d_{long} . As well, the
366 estimate (8) is usually very optimistic compared to the real optical resolu-
367 tion possible to achieve. The estimate stands for the case of perfect lens
368 focusing and the absence of any image blurring due to airplane movements
369 and camera jitters. As shown, Fig. 3, f, and Fig 8, measurements from an
370 altitude $H \simeq 1 - 1.5$ km, with $N_p \simeq 2000$, $\theta_s \simeq 45^\circ$, $\gamma = 80^\circ$, provide a
371 wave spectrum reliably defined for waves between 10-20 m to 50-60 m. The

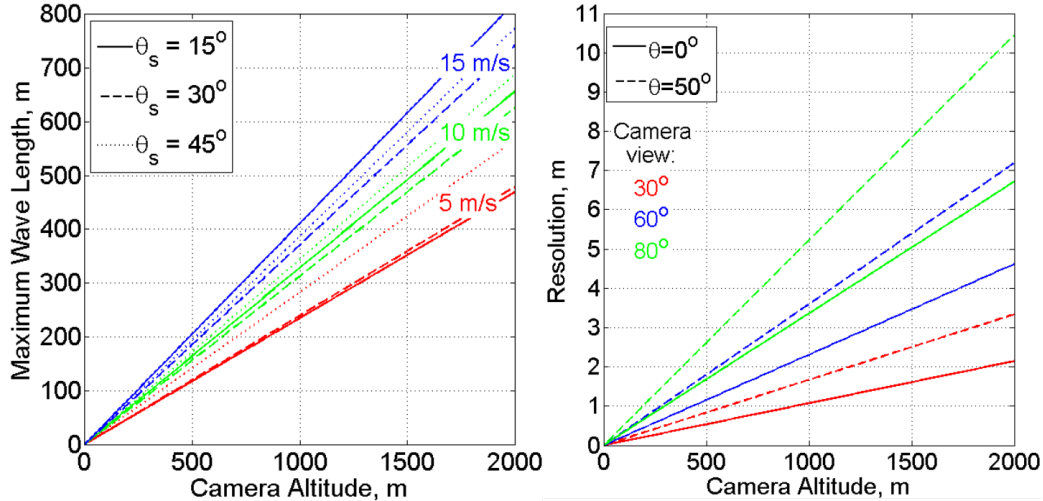


Figure 10: Left: the longest waves which can be observed within the useful part of the sunglint ($0.5 < Z_n^2/s^2 < 2$), as function of the camera altitude H . Three different sun zenith angles ($\theta_s = 15, 30, 45^\circ$) and three different wind speeds (5, 10, 15 m s^{-1}) are used for the calculations. Right: surface resolution as a function of camera altitude for the image size $N_p = 1000$ pixels, different camera view angles and two camera zenith angles ($\theta = 0^\circ$ and $\theta = 50^\circ$)

372 initial expectation gives a range between 3 m and 300 m. Nevertheless, these
 373 nominal estimates are useful to guide experiments and analysis for different
 374 conditions.

375 As a final remark, we note that, to retrieve spatio-temporal wave char-
 376 acteristics, the requirement of a perfect sunglint is less strict. Indeed, those
 377 characteristics can be derived directly from the surface brightness field and
 378 do not need the surface elevation spectrum. The previous stringent require-
 379 ments apply to robustly retrieve the wave elevation spectrum from a sunglint
 380 photograph. Other spatio-temporal wave characteristics, such as the deter-
 381 mination of a surface current-induced Doppler shift in the dispersion relation,

382 merely needs to follow individual wave crests. As such, it can be applied fur-
383 ther away from the sunglint, or even using the sky glint. Yet, a perfect
384 geolocation might be required to accurately estimate wavelengths and shifts,
385 and it is therefore recommended to work with images at small incidence
386 angles.

387 7. Conclusion

388 In this paper, the method and algorithm development are presented to
389 retrieve the two-dimensional wave spectrum from airborne sunglitter pho-
390 tographs. The implementation is demonstrated with airborne sunglitter pho-
391 tographs acquired during an experiment in the Gulf of Mexico. A linear trans-
392 fer function to relate the image brightness variations to surface elevations is
393 simply deduced from the shape of the glint. The singularity in wavenumber
394 space, inherent to this approach, is eliminated by using several image frag-
395 ments corresponding to different directions of the transfer function gradient.
396 This was earlier suggested by Bolshakov et al. (1988) and Lupyan (1988), and
397 it was also applied to satellite observations by Kudryavtsev et al. (2017a).
398 Following this methodology, the absolute wavenumber elevation spectrum
399 does not require any additional assumption or ancillary information about
400 the sky brightness, wind or wave energy.

401 As also demonstrated, a cross-correlation analysis between consecutive
402 photographs, taken with a small time lag (0.5 s), resolves the 180-degree
403 ambiguity to provide the wave direction. Further, using a transect in the
404 resulting phase spectrum gives an estimate of the wave dispersion along the
405 propagation direction. As tested, comparisons between retrieved spectra and

406 nearby NDBC buoy estimates are in good agreement, for both the spectral
407 level and energy angular distribution.

408 A case study corresponding to the wave spectral evolution with increas-
409 ing distance from shore in slanting-fetch conditions has then been considered,
410 and further provide convincing evidence of the applicability and validity of
411 the proposed method. Indeed, energy level and peak position transforma-
412 tion agree well with established approximations and laws of the wind-sea
413 development, and quantitatively compare with previous experimental data
414 and model predictions (Donelan et al., 1985; Babanin and Soloviev, 1998;
415 Ardhuin et al., 2007).

416 In the context of today’s rapidly growing technologies and the develop-
417 ment of relatively simple remote controlled measurements from drones, the
418 straightforward step-by-step proposed algorithm shall provide efficient means
419 to renew and enhance the interest of aerial photographs of ocean sunglint pat-
420 terns to infer quantitative information about surface wave characteristics and
421 related rapid transformations over coastal areas.

422 **Acknowledgment**

423 We are grateful to Fabrice Ardhuin for the help in NDBC data process-
424 ing and Vladimir Dulov for the fruitful discussions. The work was supported
425 by Russian Science Foundation via grant 15-17-20020 and at the final stage
426 via grant 17-77-30019. The support of FASO of Russia under the State
427 Assignment (No. 0827-2018-0003) and ESA SARONG project are also ac-
428 knowledged.

429 Apel, J. R., Byrne, H. M., Proni, J. R., Charnell, R. L., 1975. Observations

- 430 of oceanic internal and surface waves from the earth resources technology
431 satellite. *Journal of Geophysical Research* 80 (6), 865–881.
432 URL <http://dx.doi.org/10.1029/JC080i006p00865>
- 433 Ardhuin, F., Herbers, T. H. C., Watts, K. P., van Vledder, G. P., Jensen, R.,
434 Graber, H. C., 2007. Swell and slanting-fetch effects on wind wave growth.
435 *Journal of Physical Oceanography* 37 (4), 908–931.
436 URL <https://doi.org/10.1175/JP03039.1>
- 437 Babanin, A., Soloviev, Y., 1998. Field Investigation of Transformation of the
438 Wind Wave Frequency Spectrum with Fetch and the Stage of Development.
439 *Journal of Physical Oceanography* 28 (4), 563–576.
- 440 Barber, N. F., 1949. A Diffraction Analysis of a Photograph of the Sea.
441 *Nature* 164 (485).
- 442 Barber, N. F., Dec. 1954. Finding the Direction of Travel of Sea Waves.
443 *Nature* 174, 1048–1050.
- 444 Barrick, D. E., Lipa, B. J., 1985. Mapping surface currents. *Sea Technology*,
445 42.
- 446 Bolshakov, A. N., Burdyugov, V. M., Grodsky, S. A., Kudryavtsev, V. N.,
447 1988. The spectrum of energy containing surface waves as derived from
448 sun glitter images. *Issledovaniye Zemli iz Kosmosa* 5, 11–18.
- 449 Breon, F. M., Henriot, N., 2006. Spaceborne observations of ocean glint re-
450 flectance and modeling of wave slope distributions. *Journal of Geophysical*
451 *Research: Oceans* 111 (C6), n/a–n/a, c06005.
452 URL <http://dx.doi.org/10.1029/2005JC003343>

- 453 Caudal, G., Hauser, D., Valentin, R., Gac, C. L., 2014. Kuros: A new air-
454 borne ku-band doppler radar for observation of surfaces. *Journal of Atmo-
455 spheric and Oceanic Technology* 31 (10), 2223–2245.
456 URL <https://doi.org/10.1175/JTECH-D-14-00013.1>
- 457 Cox, C., Munk, W., 1956. Slopes of the sea surface deduced from photographs
458 of sun glitter. *Bulletin of the Scripps Institution of Oceanography* 6 (9),
459 401–488.
- 460 D’Asaro, E. A., Shcherbina, A. Y., Klymak, J. M., Molemaker, J., Novelli,
461 G., Guigand, C. M., Haza, A. C., Haus, B. K., Ryan, E. H., Jacobs, G. A.,
462 Huntley, H. S., Laxague, N. J. M., Chen, S., Judt, F., McWilliams, J. C.,
463 Barkan, R., Kirwan, A. D., Poje, A. C., Özgökmen, T. M., 2018. Ocean
464 convergence and the dispersion of flotsam. *Proceedings of the National
465 Academy of Sciences*.
466 URL <http://www.pnas.org/content/early/2018/01/09/1718453115>
- 467 Davidan, I. N., 1980. Investigation of wave probability structure on field data.
468 *GOIN 151 151*, 8–26.
- 469 De Michele, M., Leprince, S., Thiebot, J., Raucoules, D., Binet, R., 07 2012.
470 Measurement of ocean waves velocity fields from a single spot-5 dataset
471 using correlation between panchromatic and multispectral bands. *Remote
472 Sensing of Environment* 199, 266–271.
- 473 Dobson, F., Perrie?, W., Toulany, B., 03 1989. On the deep-water fetch laws
474 for wind?generated surface gravity waves. *Atmosphere-Ocean* 27, 210–236.

- 475 Donelan, M., Hamilton, J., Hui, W., 1985. Directional spectra of wind-
476 generated ocean waves. *Philosophical Transactions of the Royal Society of*
477 *London A: Mathematical, Physical and Engineering Sciences* 315 (1534),
478 509–562.
479 URL <http://rsta.royalsocietypublishing.org/content/315/1534/509>
- 480 Dugan, J., Piotrowski, C., 02 2003. Surface current measurements using air-
481 borne visible image time series 84, 309–319.
- 482 Ewans, K., C. Kibblewhite, A., 09 1990. An examination of fetch-limited
483 wave growth off the west coast of new zealand by a comparison with the
484 jonswap results. *Journal of Physical Oceanography - J PHYS OCEANOGR*
485 20, 1278–1296.
- 486 Hennings, I., Matthews, J., Metzner, M., 1994. Sun glitter radiance and radar
487 cross-section modulations of the sea bed. *Journal of Geophysical Research:*
488 *Oceans* 99 (C8), 16303–16326.
489 URL <http://dx.doi.org/10.1029/93JC02777>
- 490 Herbers, T. H. C., Jessen, P. F., Janssen, T. T., Colbert, D. B., MacMahan,
491 J. H., 2012. Observing ocean surface waves with gps-tracked buoys. *Journal*
492 *of Atmospheric and Oceanic Technology* 29 (7), 944–959.
493 URL <https://doi.org/10.1175/JTECH-D-11-00128.1>
- 494 Kahma, K., 10 1981. A study of the growth of the wave spectrum with fetch.
495 *Journal of Physical Oceanography* 11, 1503–1515.
- 496 Kudryavtsev, V., Myasoedov, A., Chapron, B., Johannessen, J. A., Col-
497 lard, F., 2012. Imaging mesoscale upper ocean dynamics using synthetic

- 498 aperture radar and optical data. *Journal of Geophysical Research: Oceans*
499 117 (C4), n/a–n/a, c04029.
500 URL <http://dx.doi.org/10.1029/2011JC007492>
- 501 Kudryavtsev, V., Myasoedov, A., Chapron, B., Johannessen, J. A., Collard,
502 F., 2012. Joint sun-glitter and radar imagery of surface slicks. *Remote*
503 *Sensing of Environment* 120 (Supplement C), 123 – 132, the Sentinel
504 Missions - New Opportunities for Science.
505 URL <http://www.sciencedirect.com/science/article/pii/S0034425712000831>
- 506 Kudryavtsev, V., Yurovskaya, M., Chapron, B., Collard, F., Donlon, C.,
507 2017a. Sun glitter imagery of ocean surface waves. Part 1: Directional spec-
508 trum retrieval and validation. *Journal of Geophysical Research: Oceans*
509 122 (2), 1369–1383.
- 510 Kudryavtsev, V., Yurovskaya, M., Chapron, B., Collard, F., Donlon, C.,
511 2017b. Sun glitter imagery of surface waves. Part 2: Waves transformation
512 on ocean currents. *Journal of Geophysical Research: Oceans* 122 (2), 1384–
513 1399.
- 514 Lupyan, E. A., 1988. Retrieval of the angular energy distribution of two-
515 dimensional elevation spectrum from optical image of the sea surface. *Issle-*
516 *dovaniye Zemli iz Kosmosa* 3, 31–35.
- 517 Lygre, A., Krogstad, H. E., 1986. Maximum entropy estimation of the
518 directional distribution in ocean wave spectra. *Journal of Physical*
519 *Oceanography* 16 (12), 2052–2060.
520 URL [https://doi.org/10.1175/1520-0485\(1986\)016<2052:MEE0TD>2.0.CO;2](https://doi.org/10.1175/1520-0485(1986)016<2052:MEE0TD>2.0.CO;2)

- 521 Melville, W. K., Lenain, L., Cayan, D. R., Kahru, M., Kleissl, J. P., Linden,
522 P. F., Statom, N. M., 2016. The modular aerial sensing system. *Journal of*
523 *Atmospheric and Oceanic Technology* 33 (6), 1169–1184.
524 URL <https://doi.org/10.1175/JTECH-D-15-0067.1>
- 525 Monaldo, F. M., Kasevich, R. S., 1981. Daylight imagery of ocean surface
526 waves for wave spectra. *Journal of Physical Oceanography* 11 (2), 272–283.
527 URL [https://doi.org/10.1175/1520-0485\(1981\)011<0272:DI00SW>2.0.CO;2](https://doi.org/10.1175/1520-0485(1981)011<0272:DI00SW>2.0.CO;2)
- 528 Nieto, B., Rodrigues, G., Hessner, K., Gonsalez, B., 2004. Inversion of ma-
529 rine radar images for surface wave analysis. *Journal of Atmospheric and*
530 *Oceanic Technology* 21, 1291–1300.
- 531 Rascle, N., Molemaker, J., Mari?, L., Noguier, F., Chapron, B., Lund,
532 B., Mouche, A., 2017. Intense deformation field at oceanic front inferred
533 from directional sea surface roughness observations. *Geophysical Research*
534 *Letters* 44 (11), 5599–5608, 2017GL073473.
535 URL <http://dx.doi.org/10.1002/2017GL073473>
- 536 Rascle, N., Noguier, F., Chapron, B., Mouche, A., Ponte, A. l., 2016. Surface
537 roughness changes by finescale current gradients: Properties at multiple
538 azimuth view angles. *Journal of Physical Oceanography* 46 (12), 3681–
539 3694.
- 540 Senet, C. M., Seeman, J., Flampouris, S., Ziemer, F., 2008. Determination
541 of Bathymetric and Current Maps by the Method DiSC Based on the
542 Analysis of Nautical X-Band Radar Image Sequences of the Sea Surface.
543 *IEEE Transactions on Geoscience and Remote Sensing* 46 (8), 2267–2279.

- 544 Spooner, J., 1822. Sur la lumiere des ondes de la mer. *Corresp. Astronomique*
545 du Baron de Zach 6, 331.
- 546 Stilwell, D., 1969. Directional energy spectra of the sea from photographs.
547 *Journal of Geophysical Research* 74 (8), 1974–1986.
548 URL <http://dx.doi.org/10.1029/JB074i008p01974>
- 549 Stilwell, D., Pilon, R. O., 1974. Directional spectra of surface waves from
550 photographs. *Journal of Geophysical Research* 79 (9), 1277–1284.
551 URL <http://dx.doi.org/10.1029/JC079i009p01277>
- 552 Walsh, E. J., Vandemark, D. C., Friehe, C. A., Burns, S. P., Khelif, D., Swift,
553 R. N., Scott, J. F., 1998. Measuring sea surface mean square slope with a
554 36-ghz scanning radar altimeter. *Journal of Geophysical Research: Oceans*
555 103 (C6), 12587–12601.
556 URL <http://dx.doi.org/10.1029/97JC02443>
- 557 Wen, S. C., Zhang, D. C., Guo, P. Z., Chen, B. H., 1989. Parameters in
558 wind?wave frequency spectra and their bearings on spectrum forms and
559 growth. *Acta Oceanol. Sinica* 8, 15–39.